A MULTISCALE SPATIOTEMPORAL APPROACH FOR TRANSFERABLE IRRIGATION DETECTION

SUPPLEMENTARY MATERIALS

Terence Conlon*
Department of Mechanical Engineering
Columbia University
New York, NY, USA
terence.conlon@columbia.edu

Christopher Small
Lamont Doherty Earth Observatory
Columbia University
Palisades, NY, USA
csmall@columbia.edu

Vijay Modi
Department of Mechanical Engineering
Columbia University
New York, NY, USA
modi@columbia.edu

February 5, 2022

1 Supplementary Background

1.1 Phenology mapping by temporal endmember unmixing

Figure 1 in the main text presents a vegetation phenology map for Ethiopia created by applying a temporal mixture model to an image cube containing 16-day 250m MODIS enhanced vegetation index (EVI) imagery between June 1, 2011 and June 1, 2021. Figure S1 presents the locations of temporal endmember (tEM) extraction from the image cube transformed into principal component (PC) space. The four extracted tEMs are then used to create the phenology map via unconstrained least-squares linear unmixing per the methodology introduced in Small [2012].

Figure S2 presents the temporal mixture model inversion error and the cumulative error statistics for Figure 1. Interpreting Figure 1 and Figure S2 together reveals that the locations of highest error occur over evergreen vegetation, primarily in the southeast of Ethiopia. As the unmixing error remains low over Tigray and Amhara, the authors stipulate that Figure 1 contains an accurate assessment of vegetation cycles in the area of interest.

2 Supplementary Methods

2.1 Sentinel-2 imagery collection

Using the Descartes Labs platform, imagery mosaics are generating by collecting all Sentinel-2 imagery available within a 10-day timestep that come from 100km-by-100km granules with less than 10% aggregate cloud cover. These images are then sorted by cloud cover and masked using the cloud masks provided by the Sen2Cor algorithm [Main-Knorn et al., 2017]. Given the 5-day revisit period of Sentinel-2 near the equator, a 10-day timestep ensures that there are two separate satellite passes per image mosaic.

Once imagery is collected for each timestep, values are assigned to individual pixels, pulling first from the image with the lowest amount of cloud cover. If there are masked pixels in this image, pixel values are determined for these locations using the image with the next lowest amount of cloud cover; this process repeats until either all the images available at a timestep are cycled through or each pixel in the 10-day mosaic is filled with valid, non-clouded values.

*Corresponding author

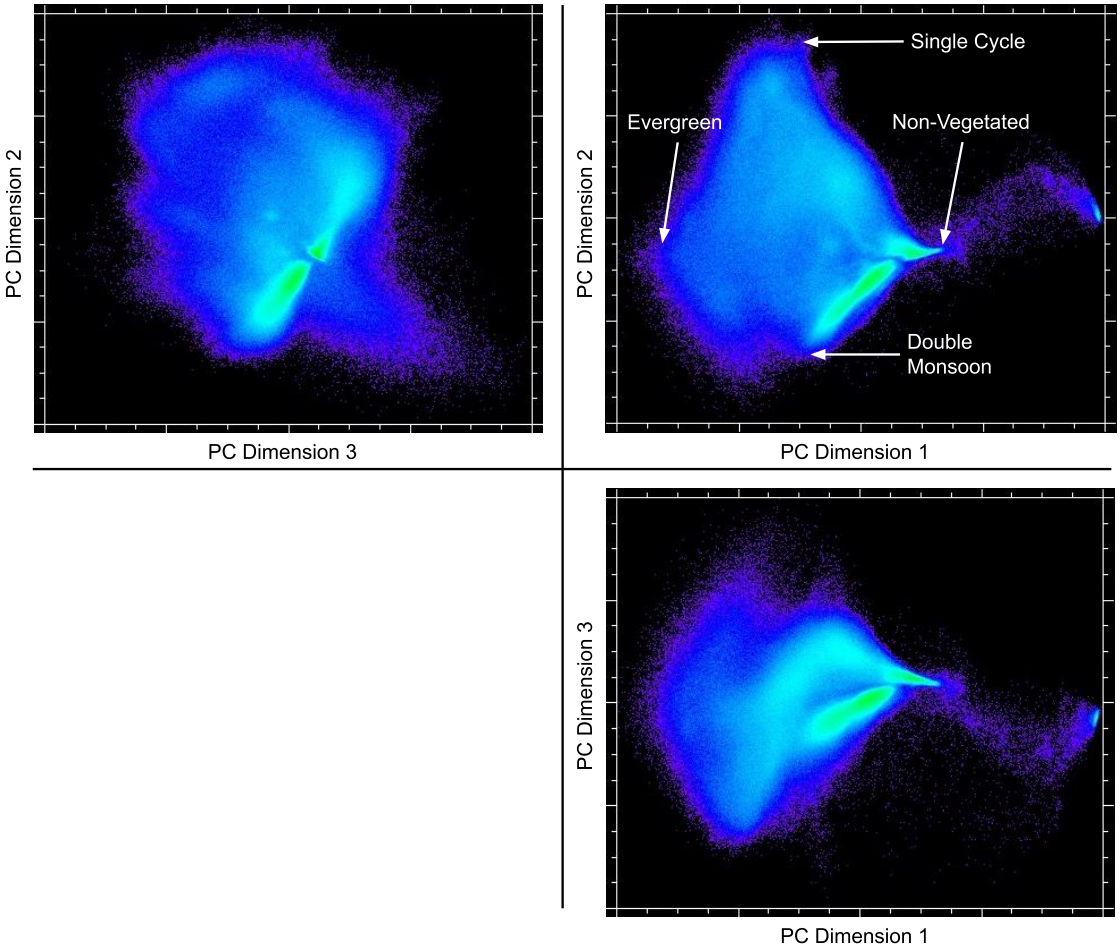

Figure S1: Views of the first three principal component (PC) dimensions of the transformed 10-year Ethiopia MODIS enhanced vegetation index (EVI) imagery cube. Locations of temporal endmembers used to construct the phenology map in Figure 1 via unconstrained linear unmixing are presented in the PC Dimension 1 vs. PC Dimension 2 plot.

For mosaics that retain invalid pixels due to persistent cloud cover across the timestep (often during the rainy season in Ethiopia, which stretches from June to September), pixel values are assigned via temporal interpolation: Each invalid pixel is given a linearly interpolated value based on the nearest preceding and subsequent image mosaic with a non-clouded value for that pixel.

Image mosaicking is performed bandwise. All 10m and 20m Sentinel-2 bands are extracted (10 bands in total); the 60m coastal aerosol and water vapor bands are ignored, as these bands contain atmospheric information not relevant for the land process monitoring task at hand. The final image processing step involves temporal smoothing of all timeseries using a 3rd order polynomial Savitzky-Golay filter with a window length of 5.

To assist with temporal interpolation of clouded pixels at the start and end of the specified time period, 82 image mosaics are collected in total – the 72 image mosaics that make up the 2 years of imagery (June 1, 2019 – June 1, 2020, and June 1, 2020 – June 1, 2021), plus 5 additional timesteps before and after the beginning and end of full time period. After interpolation and smoothing, these additional image mosaics are discarded to leave cloud-free, smoothed, 10 band Sentinel-2 imagery for only the desired 72 timesteps. The imagery is then split into annual temporal stacks, with all training and inference done on a single year's 36 timesteps of imagery.

2.2 Ground collection

The ground collection survey was conducted during the months of March and April, 2021. Enumerators collected labels across an area north and east of Lake Tana (referred to as "Tana"; see Figure 1 in the main text) in a process that

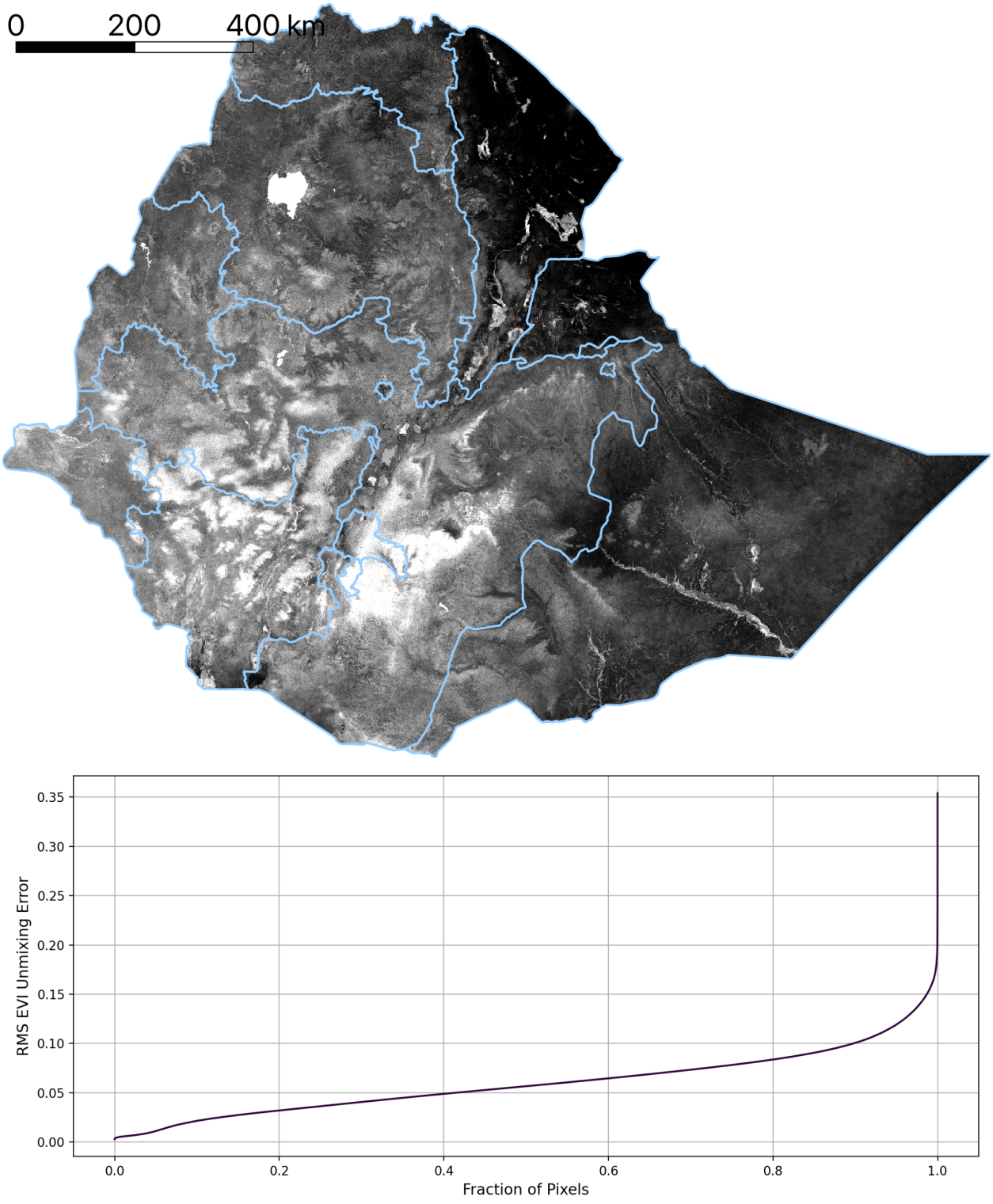

Figure S2: Root mean square (RMS) error of the temporal mixture model inversion for Figure 1. A 2% linear stretch is applied to the error map, with administrative boundaries outlined in light blue. The displayed cumulative density function shows the distribution of RMS errors for an increasing fraction of pixels in Figure 1.

involved traveling to individual plots of lands, collecting four coordinate points corresponding to the corners of the plot, and specifying whether irrigation was present on the plot during the visit. The ground collection survey team collected 2002 polygons in Tana: 1500 were labeled non-irrigated and 502 were labeled irrigated. In total, these polygons cover 1867 Ha, 78% of which was designated as non-irrigated.

2.3 Labeled data accounting

Tables S1 and S2 present summaries of the number of labeled polygons and the number of labeled samples used in this paper's analysis.

Table S1: Summary of labeled polygons, split by region and model training configuration. GC stands for ground collection labels; VC stands for visual collection labels.

		Number of Labeled Polygons							
		Training		Validation		Testing		Total	
Region	Type of Labels	Non-Irrig.	Irrig.	Non-Irrig.	Irrig.	Non-Irrig.	Irrig.	Non-Irrig.	Irrig.
Tana	GC	1050	351	225	76	225	75	1500	502
Rift	VC	12	25	3	6	3	6	18	37
Koga	VC	27	46	6	10	6	10	39	66
Kobo	VC	26	28	6	6	6	7	38	41
Alamata	VC	17	16	4	4	4	4	25	24
Liben	VC	24	25	5	5	6	6	35	36
Jiga	VC	15	13	4	3	3	3	22	19
Motta	VC	17	17	4	4	4	4	25	25
Total	GC + VC	1188	521	257	114	257	115	1702	750

Table S2: Summary of labeled samples, split by region and model training configuration. GC stands for ground collection labels; VC stands for visual collection labels.

		Number of Labeled Samples							
		Training		Validation		Testing		Total	
Region	Type of Labels	Non-Irrig.	Irrig.	Non-Irrig.	Irrig.	Non-Irrig.	Irrig.	Non-Irrig.	Irrig.
Tana	GC	63,729	24,675	14,283	5089	13,910	5361	91,922	35,125
Rift	VC	92,157	104,682	19,149	19,269	20,378	20,286	131,684	144,237
Koga	VC	150,378	98,697	29,661	23,015	27,953	24,401	207,992	146,113
Kobo	VC	93,838	123,946	30,549	36,494	31,473	48,077	155,860	208,517
Alamata	VC	58,310	21,176	14,356	4601	11,083	6447	83,749	32,224
Liben	VC	132,999	113,733	26,027	31,212	35,394	21,895	194,420	166,840
Jiga	VC	113,640	79,143	33,244	15,368	38,734	12,204	185,618	106,715
Motta	VC	94,153	47,915	34,267	11,127	27,568	9074	155,988	68,116
Total	GC + VC	799,204	613,967	201,536	146,175	206,493	147,745	1,207,233	907,887

2.4 Labeled data exploration

To better understand the vegetation phenologies contained within this study's labeled data, the similarities of EVI timeseries of the same class are explored across regions. This process first involves applying a PC transform to

all labeled training data. The samples' dimensionality is then reduced by using only the first 10 dimensions of the transformed data; these first 10 dimensions explain 91% of the variance contained within the samples' EVI timeseries.

Table S3: Pairwise pseudo-1D Kolmogorov-Smirnov (KS) statistics between regions' non-irrigated training samples. Values with typographical symbols are to be interpreted alongside Table S6.

	Tana	Rift	Koga	Kobo	Alamata	Liben	Jiga	Motta	Mean
Tana	0.00	1.13	1.85	1.00	1.25	1.69	1.50	1.33	1.39
Rift	1.13	0.00	1.48	0.62	0.71	1.43	0.95	0.57	0.98
Koga	1.85*	1.48	0.00	1.48	1.33	0.41	1.02	1.26	1.26
Kobo	1.00	0.62	1.48	0.00	0.76	1.45	1.16	0.91	1.05
Alamata	1.25	0.71	1.33	0.76	0.00	1.33	0.97	0.72	1.01†
Liben	1.69	1.43	0.41	1.45	1.33	0.00	0.91	1.23	1.21
Jiga	1.50**	0.95	1.02	1.16	0.97	0.91	0.00	0.51	1.00
Motta	1.33	0.57	1.26	0.91	0.72	1.23	0.51	0.00	0.93‡
									1.11

Table S4: Pairwise pseudo-1D Kolmogorov-Smirnov (KS) statistics between regions' irrigated training samples. Values with typographical symbols are to be interpreted alongside Table S6.

	Tana	Rift	Koga	Kobo	Alamata	Liben	Jiga	Motta	Mean
Tana	0.00	1.88	2.25	1.73	1.65	1.13	1.60	1.27	1.64
Rift	1.88	0.00	1.48	0.61	0.37	2.01	1.30	1.51	1.31
Koga	2.25*	1.48	0.00	1.37	1.45	2.46	1.98	2.20	1.88
Kobo	1.73	0.61	1.37	0.00	0.65	1.98	1.51	1.57	1.35
Alamata	1.65	0.37	1.45	0.65	0.00	1.78	1.11	1.31	1.19†
Liben	1.13	2.01	2.46	1.98	1.78	0.00	1.41	0.98	1.68
Jiga	1.60**	1.30	1.98	1.51	1.11	1.41	0.00	0.89	1.40
Motta	1.27	1.51	2.20	1.57	1.31	0.98	0.89	0.00	1.39‡
									1.48

After dimensionality reduction via the PC transform, the two sample Kolmogorov-Smirnov (KS) test statistic is calculated between sample distributions of the same class across regions. The two-sample KS statistic determines the largest absolute distance between two 1D empirical distributions, and is presented in Eq. S1:

$$D_{KS} = sup_x|F_1(x) - F_2(x)| \tag{S1}$$

where F_1 and F_2 are the two empirical distribution functions of 1D variable *x*, and *sup* is the supremum function. The KS statistic is assessed for two reasons: 1) the statistic depends on no assumptions about the underlying data distributions; and 2) the statistic has been adapted for multivariate distributions via the pseudo-1D KS metric [Hagen et al., 2020]. In this adaptation, the pseudo-1D KS metric, $D_{KS,P1D}$, is the Euclidean KS statistic calculated between successive orthogonal dimensions of two multivariate distributions:

$$D_{KS,P1D} = \sqrt{(D_{KS,1})^2 + (D_{KS,2})^2 + \cdots + (D_{KS,n})^2} \tag{S2}$$

where

$$D_{KS,n} = sup_{y_n} |F_1(y_n) - F_2(y_n)| \tag{S3}$$

Here, Eq. S3 represents the KS statistic between the empirical distribution functions F_1 and F_2 of the n^{th} dimension of multivariate variable y. As only the first 10 PC dimensions of the transformed data are used, n ranges between 1 and 10.

Table S3 presents pairwise pseuso-1D KS statistics between regions' non-irrigated samples; Table S4 presents pairwise pseuso-1D KS distances between regions' irrigated samples. Here, the relative statistics between distributions are compared, as the absolute statistics cannot be interpreted in a physically meaningful way. The cells with typographical marks in the two tables indicate statistics to be interpreted with the results in Table S6, discussed alongside that table. Tables S3 and S4 show that the relative pairwise statistic between regional distributions is larger among the irrigated sample sets, indicating that irrigated samples are more dissimilar across regions compared to the non-irrigated samples. This takeaway reflects the varying nature of irrigation practices across Ethiopia – irrigation can occur at different parts of the dry season for a variety of different crops. In contrast, the phenologies of non-irrigated cropland must mirror Ethiopia's primary rains, which are consistent in time for the regions included in this analysis.

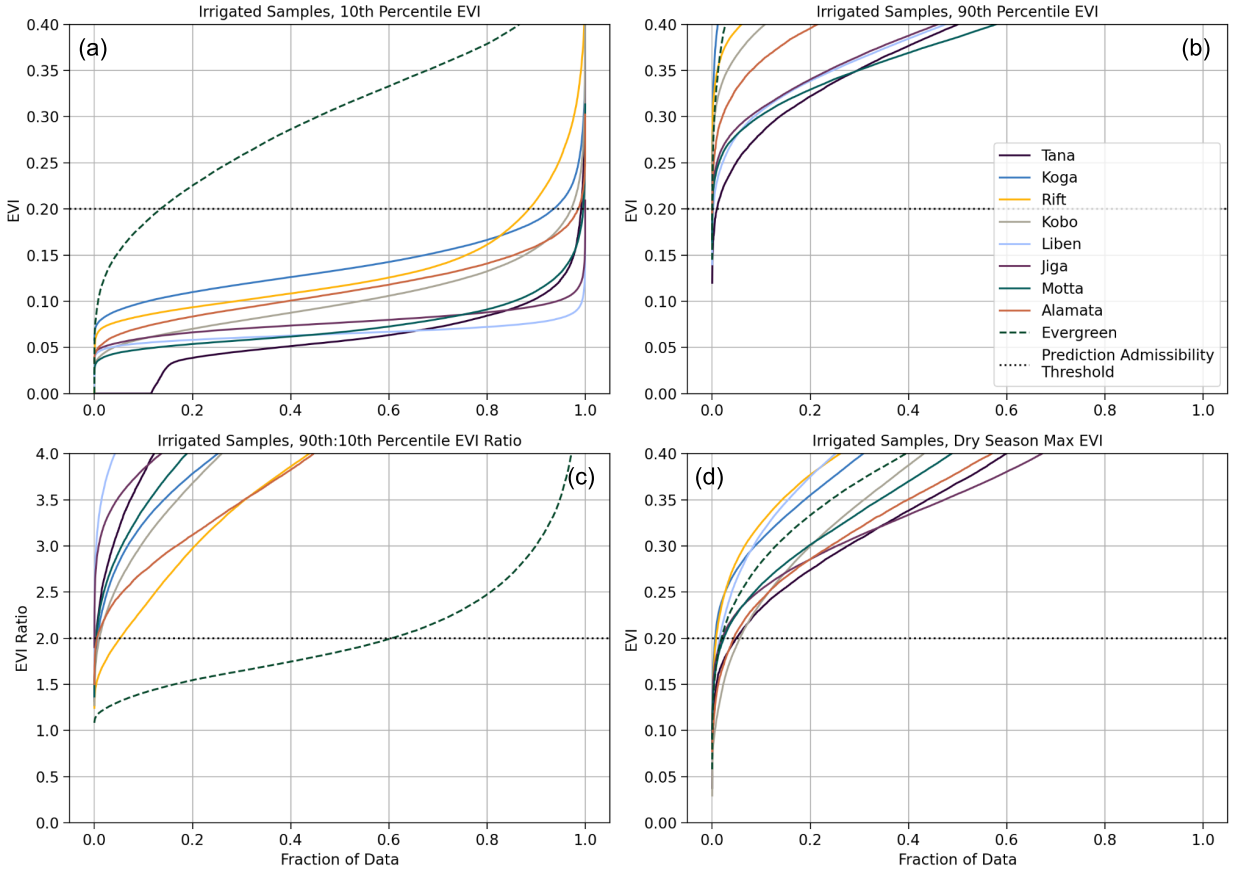

Figure S3: Cumulative distribution functions (CDFs) for the (a) 10th and (b) 90th EVI timeseries percentiles; (c) the 90th:10th EVI timeseries percentile ratio; and (d) the maximum EVI value during the dry season (December 1st, 2020, to April 1th).

2.5 Determining the prediction admissibility criteria

The prediction admissibility criteria presented in the Methodology of the main text (see Table 1) are informed by the cumulative distribution functions (CDFs) of the collected samples' EVI timeseries. By imposing admissibility criteria that closely match the distribution of the samples' EVI timeseries, heuristics are devised to exclude many pixels not relevant to the non-irrigated/irrigated cropland prediction methodology. Figure S3 presents CDFs for the 10th and 90th EVI timeseries percentiles, the 90th:10th EVI timeseries percentile ratio, and the maximum EVI value during the dry

season. Values are presented for all regions' irrigated samples only, along with a set of pixel timeseries over evergreen areas.

Figure S3(a) shows that a maximum of 0.2 for the 10^{th} percentile of the EVI timeseries is achieved by nearly all irrigated samples, and how this ceiling filters out 85% of all evergreen samples. Similarly, a minimum 90^{th}:10^{th} percentile EVI ratio of 2 is satisfied by nearly all irrigated samples and excludes 60% of evergreen samples (Figure S3(c)). While no EVI timeseries for barren or non-vegetated areas are shown in this figure, the criteria specifying a 90^{th} percentile EVI value above 0.2 and a dry season max EVI value above 0.2 are met by the vast majority of irrigated samples (Figure S3(b,d)), and would filter out many of these non-cropped pixels.

3 Supplementary Results

3.1 Evaluating the effects of randomly shifted input timeseries with a Gradient-Class Activation Map

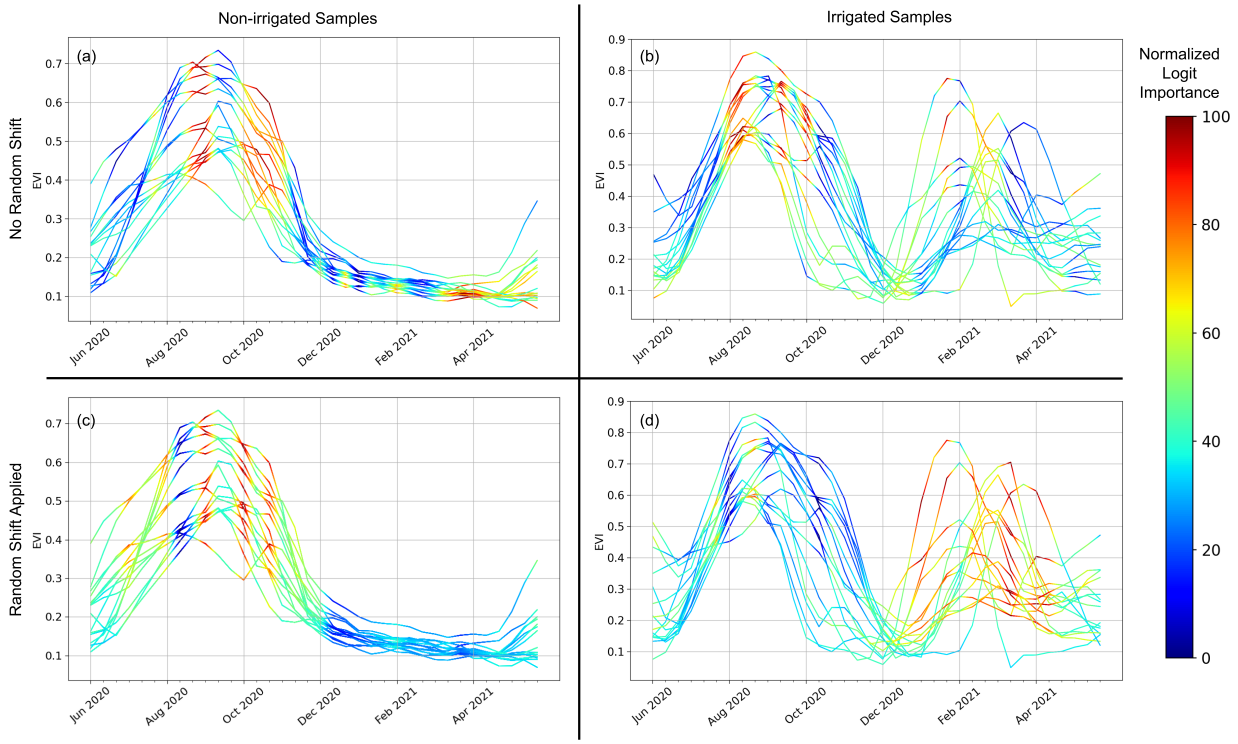

Figure S4: Modified Grad-CAM timestep importances for 16 randomly selected non-irrigated and irrigated enhanced vegetation index (EVI) timeseries from Koga, before and after the timeseries shift is applied.

Implementing a modified Gradient-Class Activation Map (Grad-CAM) for visual prediction explanation provides further evidence for improved prediction robustness from randomly shifting input EVI timeseries. A Grad-CAM uses the gradients flowing into the final layer of a neural network to produce a localization map highlighting important portions of the input for predicting a concept. Originally developed for images in Selvaraju et al. [2020], this technique can be applied analogously to timeseries. To do so, a transformer-based classifier model with its 32-node penultimate dense layer removed is trained on all VC regions' training datasets; by removing this fully connected layer, the importance of each timestep input for prediction can be visualized, as there is no longer a layer obscuring the gradient flow into the final prediction nodes. Figure S4 displays the normalized timestep prediction importances for 16 randomly selected non-irrigated and irrigated EVI timeseries from the Koga region. Results are presented for two models: the first trained without randomly shifting input timeseries, and the second trained with the random shift applied.

Figure S4 demonstrates that the input timesteps most important for prediction – displayed in red per the Normalized Logit Importance colorbar – are more continuous and better reflect a common understanding of what portions of a phenology should be predictive once the model is trained on randomly shifted input timeseries. For the non-irrigated samples, the model trained on the randomly shifted timeseries identifies a larger portion of the timesteps during the

rainy season as highly predictive (Figure S4(c)); this model also correctly identifies vegetation growth during dry season timesteps as important for identifying irrigated samples (Figure S4(d)). In comparison, the model trained on the non-shifted timeseries identifies scattered timesteps as predictive for both non-irrigated and irrigated samples (Figure S4(a,b)); it does not emphasize dry season vegetation growth as predictive of irrigation presence (Figure S4(b)). Instead, this model learns to identify isolated, non-intuitive timesteps, and as a consequence is more likely to misclassify input timeseries that differ slightly from those in the training data.

3.2 Ablation study: Limiting polygons used during training

To understand the impact of the amount of training data on model performance, an ablation study is conducted where the fraction of labeled polygons included in each region's training dataset is varied between 0.15 and 0.85; the complementary fraction of each region's polygons comprises the test dataset. For each fraction of training polygons, the CatBoost model architecture is trained on all combinations of all 7 visual collection (VC) regions' training datasets; performance is assessed on the withheld VC regions in a process identical to the one described for main text Figures 5 and 6. All models are trained on randomly shifted EVI timeseries.

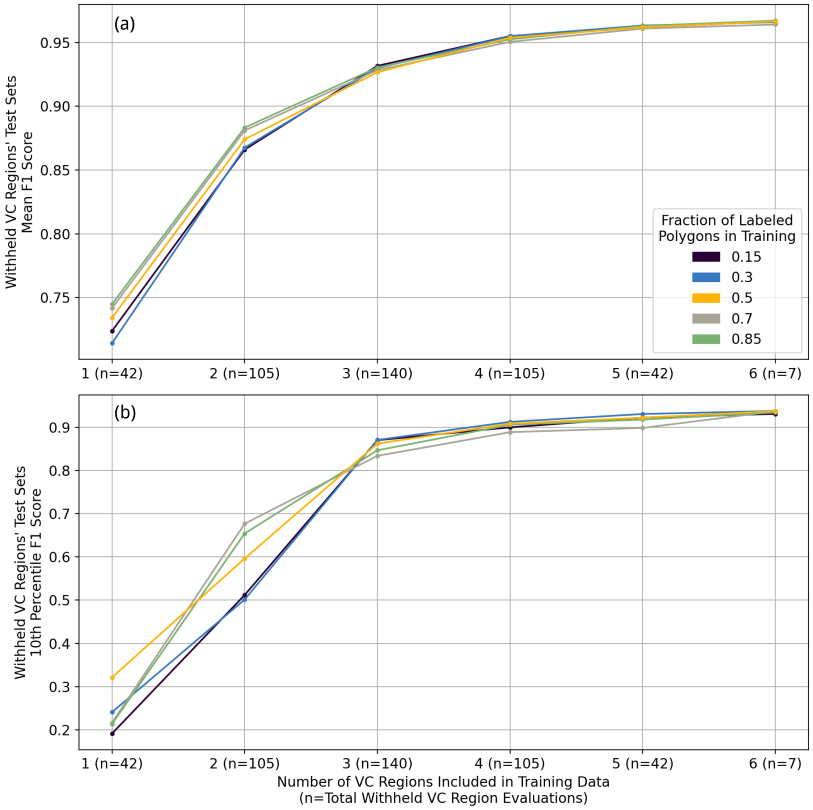

Figure S5: Withheld region test dataset performance for different fractions of labeled polygons included in the training datasets; the complementary fractions of labeled polygons constitute the test datasets. Predictions are made using a CatBoost model architecture. (a) presents mean F1 score over the withheld regions; (b) presents the 10th percentile F1 score over the withheld regions.

Figure S5 presents the results of this ablation study, in which minimal impact is observed when varying the fraction of polygons included in each region's training dataset between 0.15 and 0.85. On average, withheld region F1 score decreases by approximately 0.05 as the fraction of training polygons drops from 0.85 to 0.15 when 1 VC region is included in the training data; this gap shrinks as additional VC regions are incorporated during training, becoming negligible for all models trained on 3 or more VC regions' data. A larger performance delta among the 10th percentile of withheld regions' F1 scores exists when fewer than 3 VC regions are included during training; similar to the average performance metrics, this gap collapses when the classification model is trained on labeled data from 3 or more VC regions.

Figure S5 demonstrates that the irrigation prediction models are robust even when limiting the fraction of polygons included in training datasets to 15% of the total. Here, the inclusion of labeled data from multiple regions and randomly shifting the EVI timeseries inputs introduces enough variance to the classification model during training so that performance over regions unseen by the classifier remains high.

3.3 Comparison of predictions across model architectures

To ensure that different irrigation detection architectures converge on similar decision boundaries, the alignment of predictions across the transformer-based and CatBoost models is investigated. Here, both architectures are training on the randomly shifted EVI timeseries of all 7 VC regions' training datasets; predictions are then made over all labeled samples. Table S5 presents the alignment of these predictions, showing a high degree of prediction similarity: An average regional prediction alignment of 98.9% is calculated. The close alignment of predictions made by both these models expands the basis for the solution set.

Table S5: Comparison between Transformer and CatBoost model predictions for models trained on all 7 visual collection (VC) regions' training datasets.

Region	Type of Labels	Num. Aligned Sample Predictions		Num. Misaligned Sample Predictions		Fraction of aligned predictions
		Non-Irrig. (0)	Irrig. (1)	Transformer: 0 CatBoost: 1	Transformer: 1 CatBoost: 0	
Tana	GC	88,587	35,035	728	2690	0.973
Rift	VC	130,399	142,114	2367	1024	0.988
Koga	VC	207,536	144,284	1401	827	0.994
Kobo	VC	156,946	203,510	2313	583	0.992
Alamata	VC	84,024	31,978	615	251	0.993
Liben	VC	193,428	165,933	884	971	0.995
Jiga	VC	184,116	106,384	955	833	0.994
Motta	VC	155,056	65,956	1689	1363	0.986

3.4 Determining the relative importance of each visual collection region

Through a pair of ordinary least-squares (OLS) regressions, the contribution of each VC region to target region performance can be assessed. Table S6 presents OLS regression coefficients and P-values on target region F1 scores for the 7 VC regions used during training, where the F1 scores are collected over all withheld regions for all transformer classifier models presented in Figure 6 of the main text. In interpreting the regression results, variables with P-values above 0.05 are considered not statistically significant.

Table S6 shows that training data from the regions of Alamata or Kobo have the largest impact on Tana test dataset performance, increasing F1 score on average by 0.032 or 0.024, respectively. The non-statistically significant contributions of Koga and Jiga's training data to Tana test dataset performance are highlighted, shown by the values marked with * and **. Comparing these non-statistically significant results with the relevant cells in Tables S3 and S4 – also marked with * and ** – reveals that non-irrigated and irrigated samples from both Koga and Jiga are more dissimilar from Tana labeled samples compared to the regional average, determined by the KS distance between the regions' data.

Table S6 also shows that the inclusion of labeled samples from Motta and Alamata during training causes the largest increase in F1 score over the withheld VC regions; these increases, shown by values marked with † and ‡, amount to 0.08 and 0.071, respectively. Again, comparing these data points to the KS distances marked with † and ‡ in Tables S3 and S4 demonstrates that non-irrigated and irrigated samples from Motta and Alamata are more similar to withheld VC regions' labeled data on average, as compared to samples from other VC regions.

Taken together, the results from Tables S3, S4, and S6 yield the intuitive finding that labeled samples more similar to those in a target region have a greater positive impact on performance, while more dissimilar labeled samples have a weaker effect on performance.

Table S6: Ordinary least squares regression on withheld target region F1 scores. F1 scores are collected over all withheld regions for all transformer classifier models presented in Figure 6 of the main text. Values with typographical symbols are to be interpreted alongside Tables S3 and S4.

	Tana (R^2=0.317, n=127)		Withheld VC Regions (R^2=0.18, n=441)	
Source VC Region	Coefficient	P-value	Coefficient	P-value
Rift	0.018	0.008	-0.012	0.327
Koga	0.013*	0.056*	0.016	0.172
Kobo	0.024	0.001	0.029	0.016
Alamata	0.032	0.000	0.071†	0.000†
Liben	-0.011	0.122	0.028	0.019
Jiga	0.013**	0.063**	0.047	0.000
Motta	0.016	0.024	0.080‡	0.000‡

3.5 Independently labeled polygons for performance assessment at inference

Figure S6 presents the centroids of all polygons collected by additional enumerators for prediction performance assessment at model inference. Non-irrigated polygon locations are shown in red and irrigated polygons locations are shown in blue.

References

Christopher Small. Spatiotemporal dimensionality and Time-Space characterization of multitemporal imagery. *Remote Sensing of Environment*, 124:793–809, 2012. ISSN 00344257. doi:10.1016/j.rse.2012.05.031. URL `http://dx.doi.org/10.1016/j.rse.2012.05.031`.

Magdalena Main-Knorn, Bringfried Pflug, Jerome Louis, Vincent Debaecker, Uwe Müller-Wilm, and Ferran Gascon. Sen2Cor for Sentinel-2. In Lorenzo Bruzzone, editor, *Image and Signal Processing for Remote Sensing XXIII*, volume 10427, pages 37–48. International Society for Optics and Photonics, SPIE, 2017. doi:10.1117/12.2278218. URL `https://doi.org/10.1117/12.2278218`.

Alex Hagen, Jan Strube, Isabel Haide, James Kahn, Shane Jackson, and Connor Hainje. A Proposed High Dimensional Kolmogorov-Smirnov Distance. *Machine Learning and the Physical Sciences: Workshop at the 34th Conference on Neural Information Processing Systems (NeurIPS)*, (NeurIPS):1–6, 2020. URL `https://ml4physicalsciences.github.io/2020/`.

Ramprasaath R. Selvaraju, Michael Cogswell, Abhishek Das, Ramakrishna Vedantam, Devi Parikh, and Dhruv Batra. Grad-CAM: Visual Explanations from Deep Networks via Gradient-Based Localization. *International Journal of Computer Vision*, 128(2):336–359, 2020. ISSN 15731405. doi:10.1007/s11263-019-01228-7.

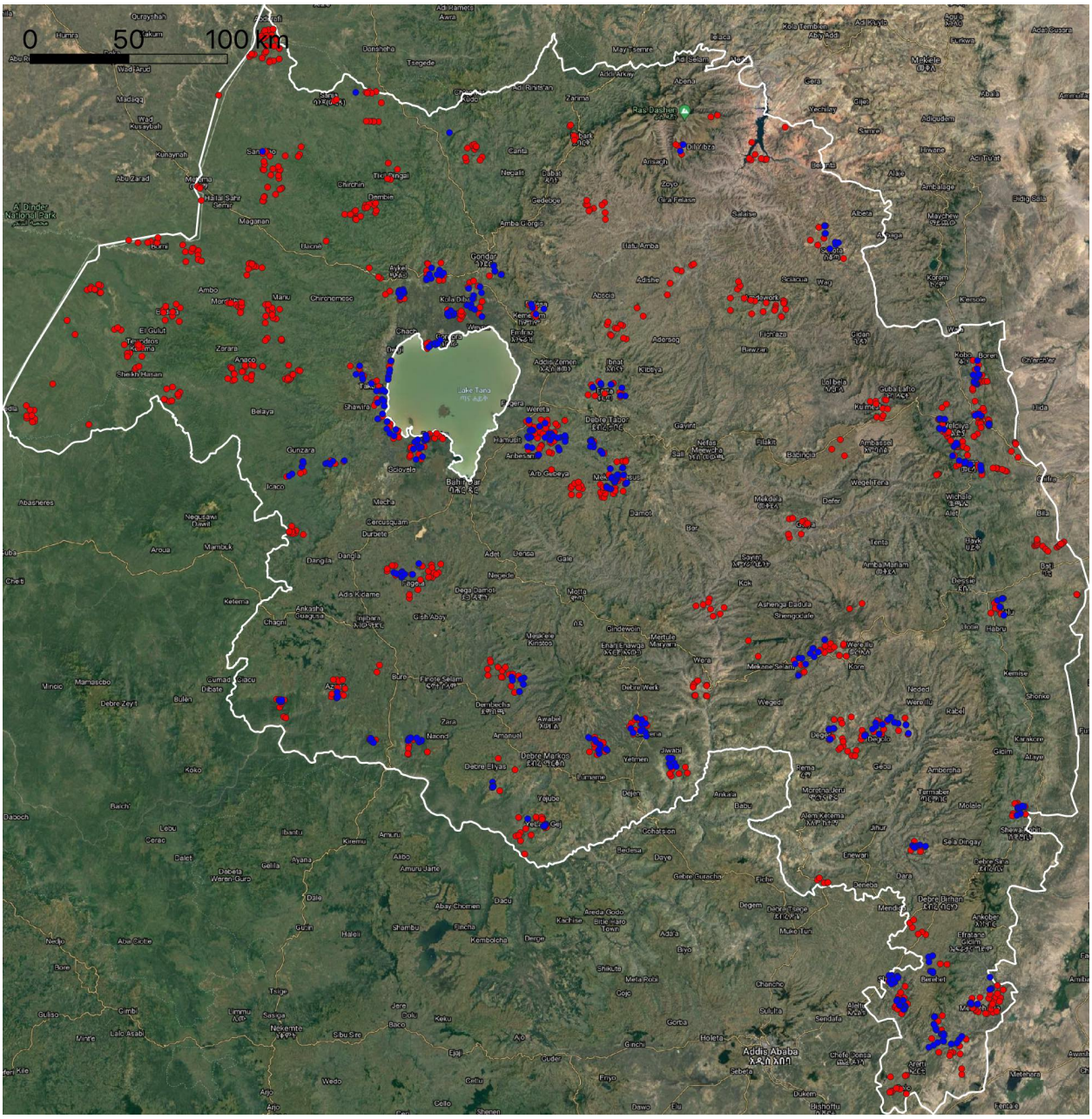

Figure S6: Locations of independently labeled polygons for additional model performance assessment. The centroids of non-irrigated polygons are shown in red, 1082 in total; the centroids of irrigated polygons are shown in blue, 519 in total. These polygons produce 361,451 non-irrigated samples and 48,465 irrigated timeseries samples.

Appendix A

Appendix A presents labeled samples before and after cluster cleaning for all label collection regions except Koga, which is presented in Figure 3 of the main text.

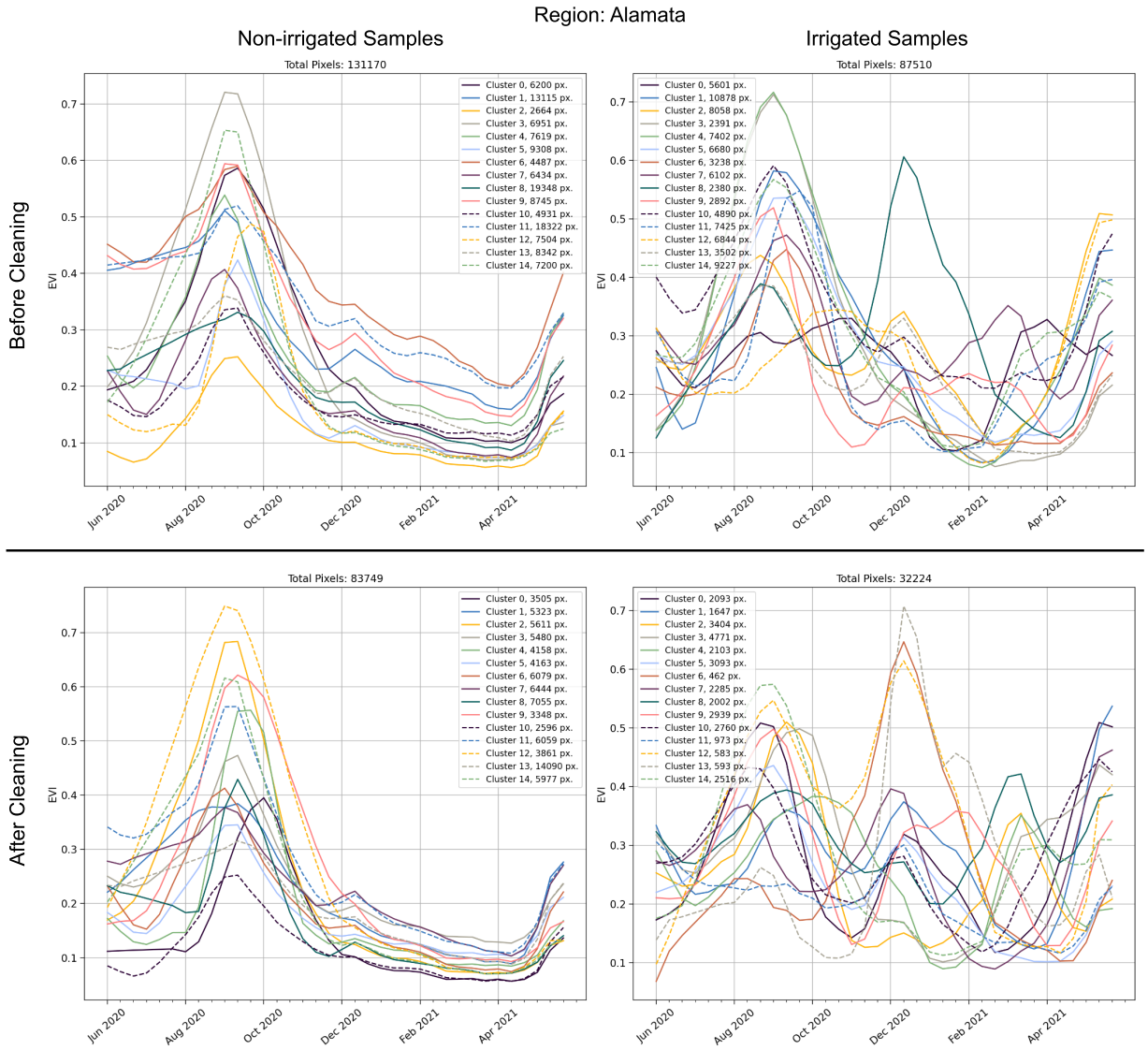

Figure S7: Clustered enhanced vegetation index (EVI) timeseries before and after cluster cleaning for the Alamata region. After cleaning, all non-irrigated clusters display a single vegetation peak aligned with the main rainy season, and the irrigated clusters all display a vegetation cycle during the dry season.

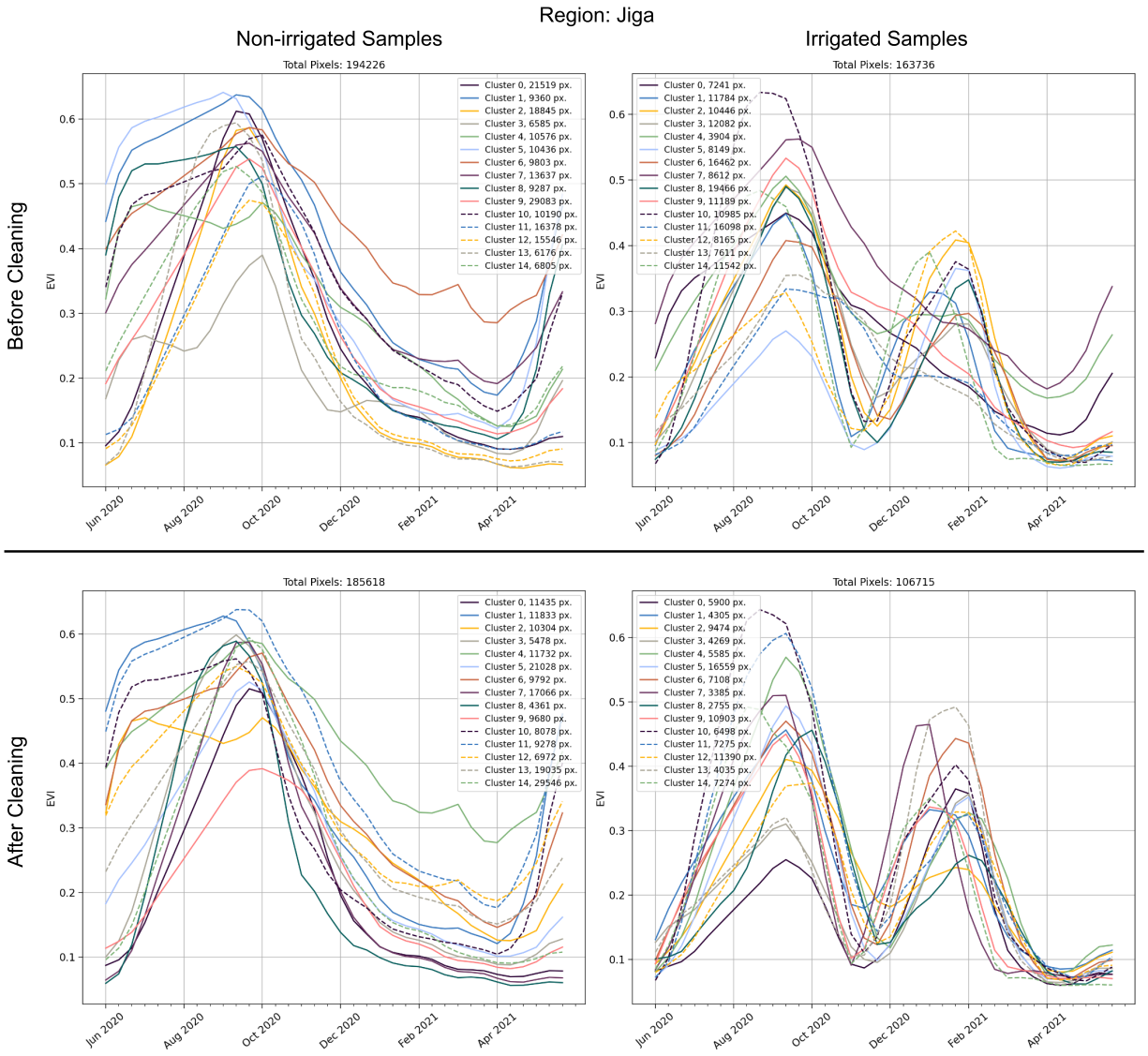

Figure S8: Clustered enhanced vegetation index (EVI) timeseries before and after cluster cleaning for the Jiga region. After cleaning, all non-irrigated clusters display a single vegetation peak aligned with the main rainy season, and the irrigated clusters all display a vegetation cycle during the dry season.

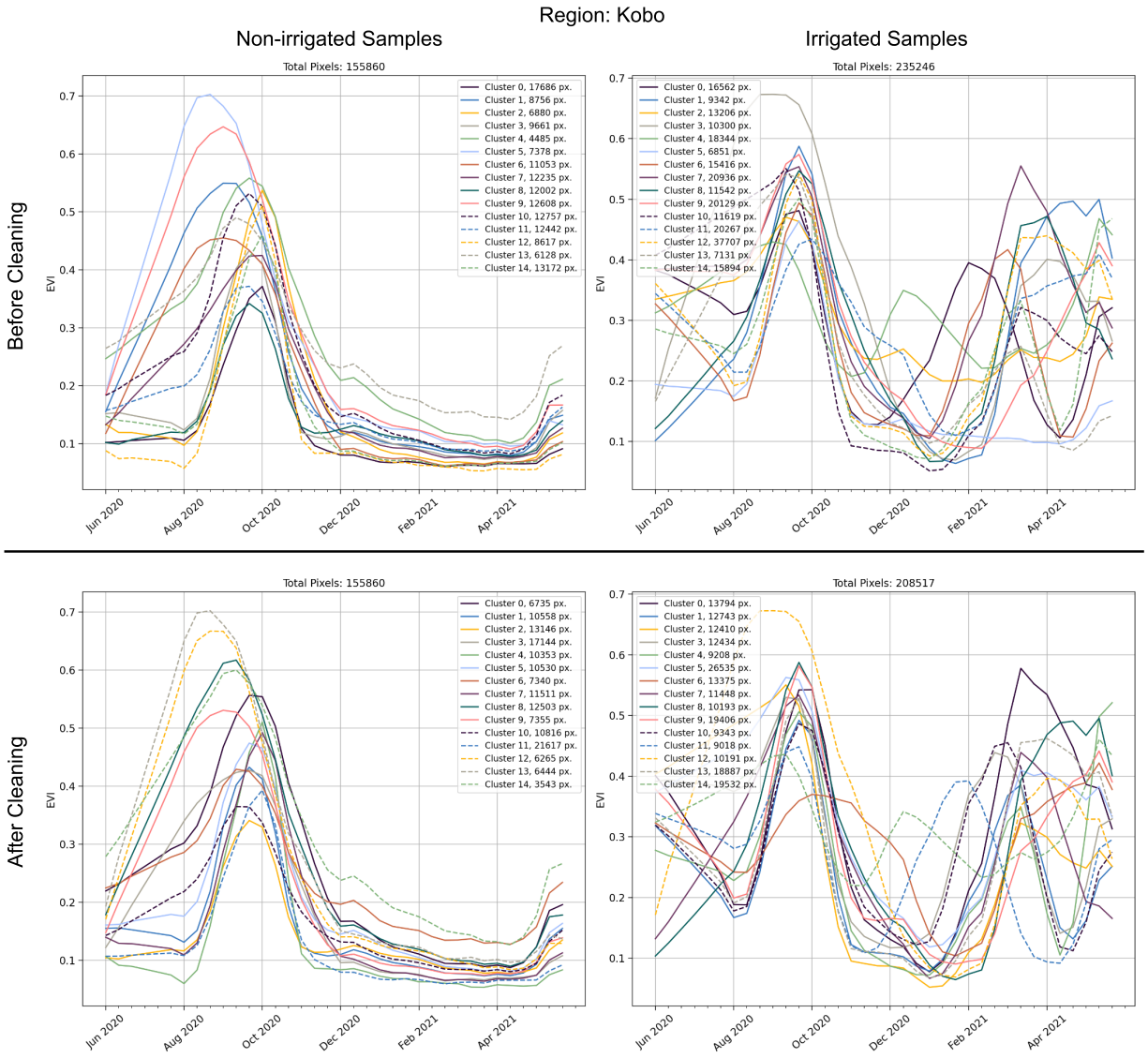

Figure S9: Clustered enhanced vegetation index (EVI) timeseries before and after cluster cleaning for the Kobo region. After cleaning, all non-irrigated clusters display a single vegetation peak aligned with the main rainy season, and the irrigated clusters all display a vegetation cycle during the dry season.

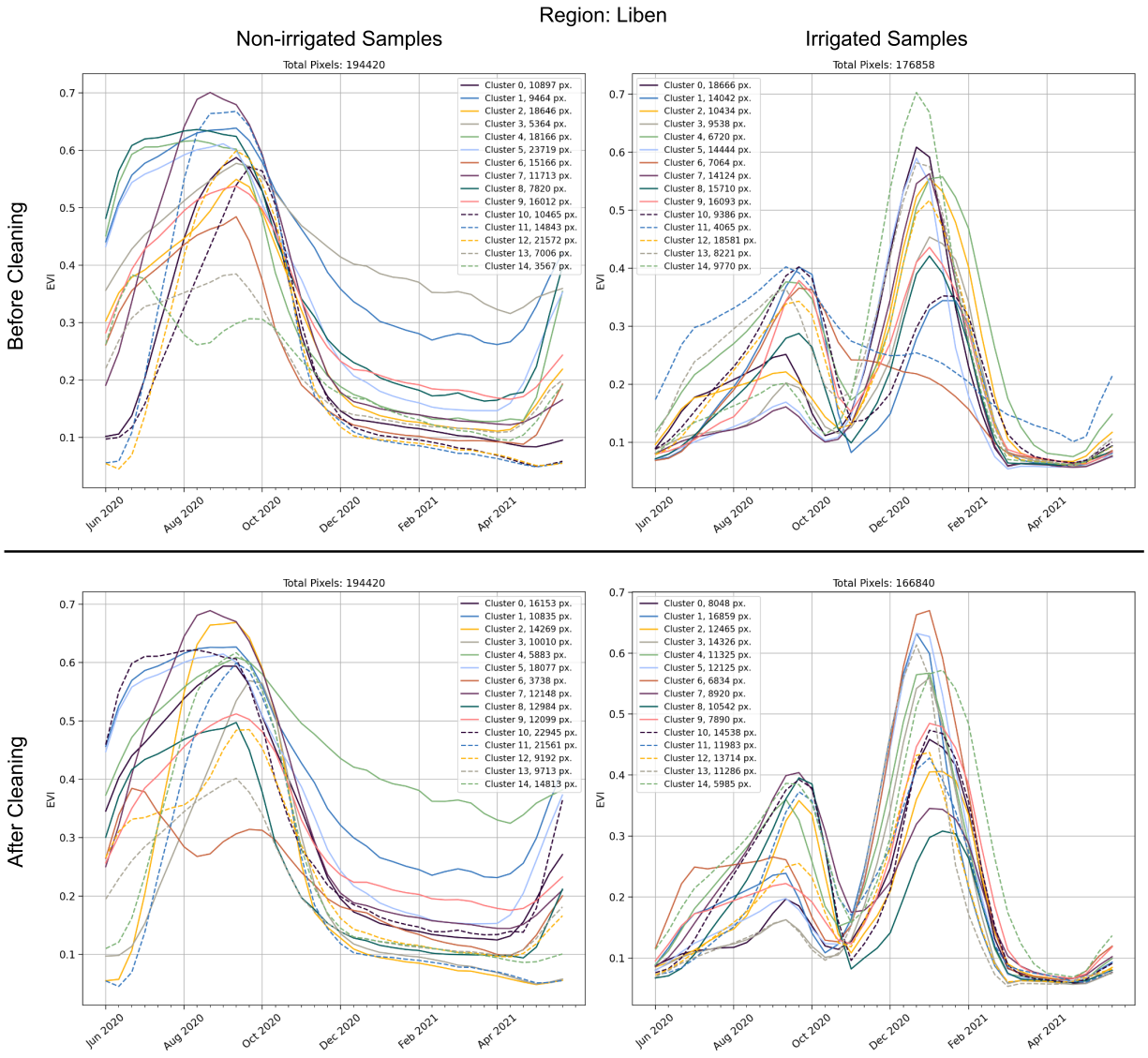

Figure S10: Clustered enhanced vegetation index (EVI) timeseries before and after cluster cleaning for the Liben region. After cleaning, all non-irrigated clusters display a single vegetation peak aligned with the main rainy season, and the irrigated clusters all display a vegetation cycle during the dry season.

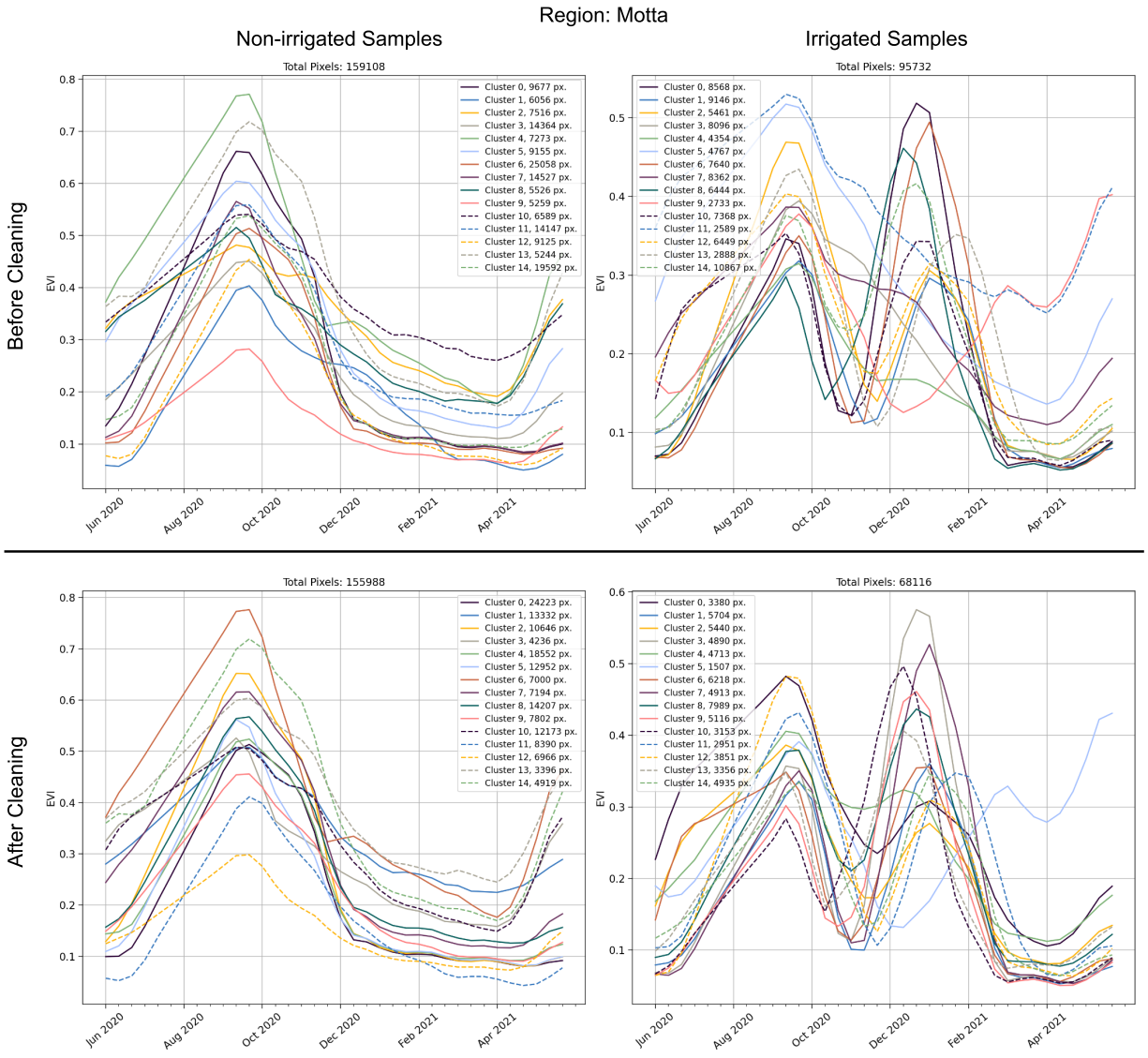

Figure S11: Clustered enhanced vegetation index (EVI) timeseries before and after cluster cleaning for the Motta region. After cleaning, all non-irrigated clusters display a single vegetation peak aligned with the main rainy season, and the irrigated clusters all display a vegetation cycle during the dry season.

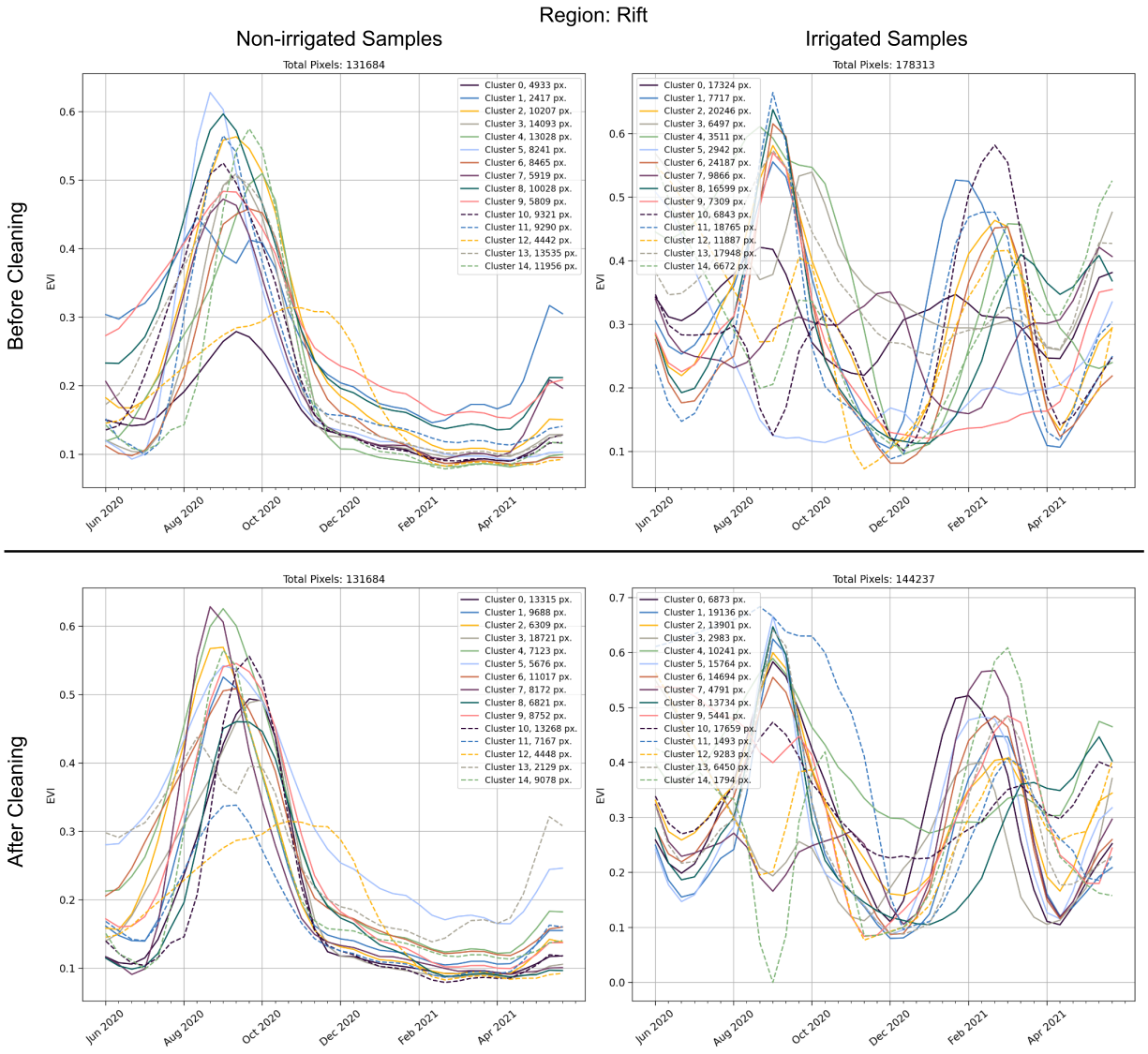

Figure S12: Clustered enhanced vegetation index (EVI) timeseries before and after cluster cleaning for the Rift region. After cleaning, all non-irrigated clusters display a single vegetation peak aligned with the main rainy season, and the irrigated clusters all display a vegetation cycle during the dry season.

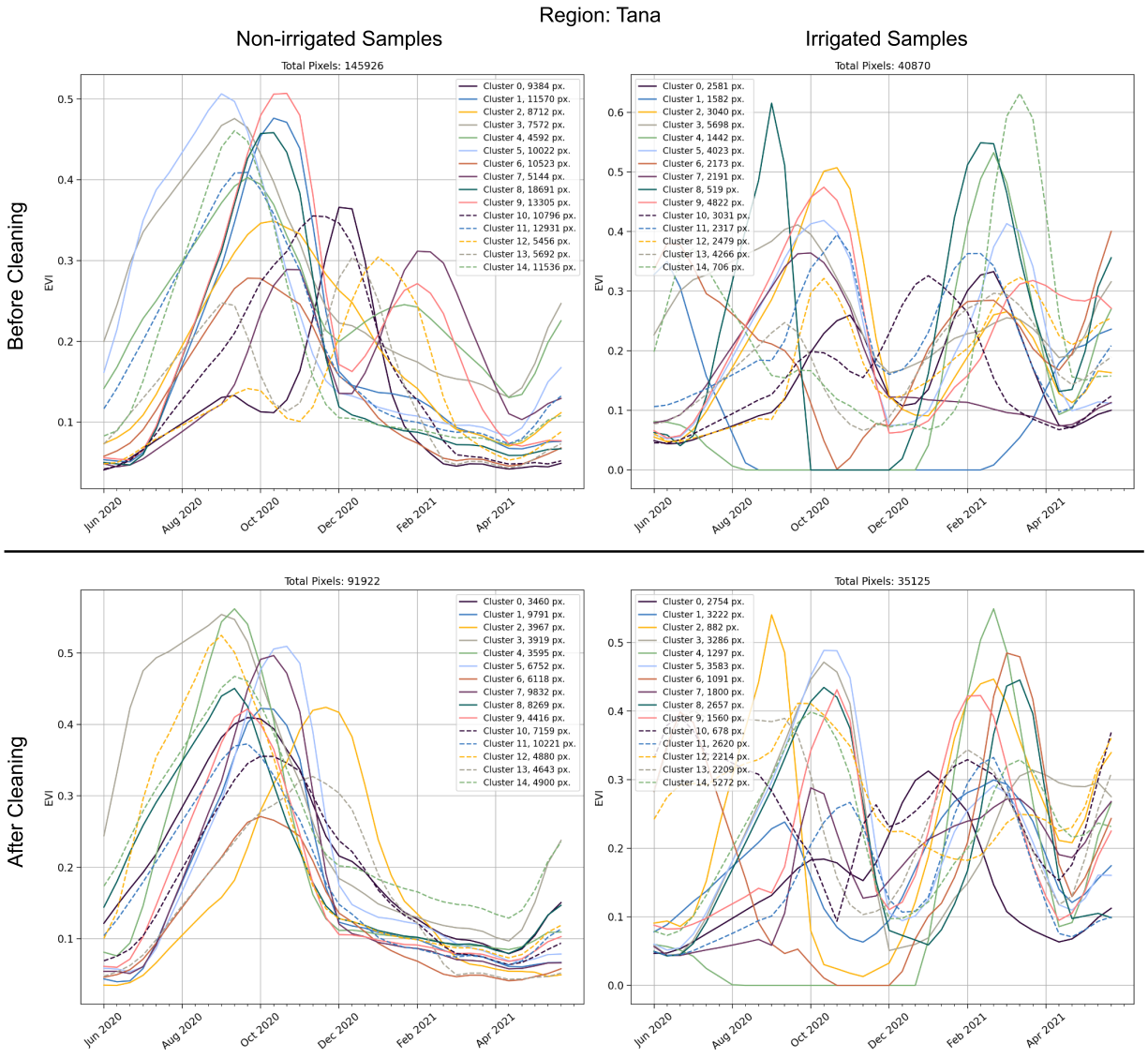

Figure S13: Clustered enhanced vegetation index (EVI) timeseries before and after cluster cleaning for the Tana region. After cleaning, all non-irrigated clusters display a single vegetation peak aligned with the main rainy season, and the irrigated clusters all display a vegetation cycle during the dry season.